Journal of Sound and Vibration 537 (2022) 117196

Contents lists available at ScienceDirect

Journal of Sound and Vibration

journal homepage: www.elsevier.com/locate/jsvi

Towards phase-based defect detection: A feasibility study in vibrating panels

F. Cosco [a,b,c,*], J. Cuenca [b], W. Desmet [c,d], K. Janssens [b], D. Mundo [a]

[a] Department of Mechanical, Energy and Management Eng., University of Calabria, Via P. Bucci, Cubo 46C, Rende, 87036, Italy
[b] Siemens Industry Software NV, Interleuvenlaan 68, Leuven, B-3001, Belgium
[c] LMSD Division, KU Leuven, Celestijnenlaan 300, Heverlee, B-3001, Belgium
[d] Dynamics of Mechanical and Mechatronic Systems, Flanders Make, Belgium

ARTICLE INFO

Keywords:
Non-contact measurements
Full-field measurements
Video processing
Motion magnification
Damage detection

ABSTRACT

This work discusses the possibility of using phase-based motion magnification as a non-destructive inspection tool for defect detection and identification in vibrating panels. Phase-based motion magnification has recently emerged as a potentially disruptive technology in the field of optical methods for vibration engineering. In fact, the method allows to post-process high-speed video recordings in order to magnify small motions happening in a prescribed bandwidth. In particular, our strategy relies on measuring the full-field low-frequency eigenshapes, and extracting their aberration as resulting from small defects. Effects of defects are usually very localized in space but may appear even at lower frequencies, making the approach particularly suitable for any kind of high-resolution full-field optical technique. Within this work, a novel phase-based processing pipeline for defect detection is described, and a set of preliminary tests is discussed to assess the feasibility and advantages of the methodology. All validations were carried out by means of numerical simulations relying upon a photo-realistic dynamic finite element model of a rectangular plate.

1. Introduction

In the last few decades, image-based optical methods have emerged as an attractive solution for measuring vibrations due to exceptional advances in computing power, memory storage and increased availability of high-speed camera sensors [1]. Besides the industrial-grade optical non-destructive methods such as laser Doppler vibrometry (LDV) [2–5] or electronic speckle pattern interferometry (ESPI) [2,6], novel image-based measuring techniques are emerging, which rely on images or photographs to sense measurable quantities for structural dynamics and vibration monitoring.

Recent trends are characterized by migrating or adapting well-established computer vision techniques to high-speed imaging for vibration monitoring applications: this trend has been fueled mostly by technological developments, with modern hardware making old methods suitable for dynamic applications. An emblematic example is optical-flow. Its theory dates back to the early eighties [7–9], but it was recently demonstrated as a viable tool for modal analysis [10–12], structural vibration measurements [13], and even damping identification [14]. Similarly, although the principles of stereo or multi-view photogrammetry have matured in the last century, a plethora of photogrammetry methodologies have appeared recently for structural dynamics [1]. Methods can be broadly classified into three categories, depending on the tracking approach used: point-tracking (PT) [3,4,15–18], digital image correlation (DIC) [3,5,6,19–27], and target-less approaches. Stereo Photogrammetry principles have been recently adopted for achieving 3D

* Corresponding author at: Department of Mechanical, Energy and Management Eng., University of Calabria, Via P. Bucci, Cubo 46C, Rende, 87036, Italy.
E-mail address: francesco.cosco@unical.it (F. Cosco).

https://doi.org/10.1016/j.jsv.2022.117196
Received 9 September 2021; Received in revised form 6 July 2022; Accepted 14 July 2022
Available online 28 July 2022

vibration measures combining a single high-speed camera with a simpler mass-market still camera [28], whereas the pros and cons of a multi-view approach have been recently discussed in [29]. The interested reader may find a broader review of the last decades' advances on optical methods in [30].

A peculiar alternative to all the above-mentioned methods relies on the video motion magnification (VMM) approach. Originally introduced at MIT [31–34], VMM relies on a phase-based Eulerian video processing approach consisting of magnifying motion happening in a prescribed frequency band. Fueled by its unprecedented ability of magnifying motion without increasing also the noise floor, several methods flourished which adopted VMM as a pre-processor in combination with other techniques, for exploiting the resulting increase of the overall signal-to-noise ratio. In [35] operational deflection shapes are extracted using VMM in combination with PT; another joint method combining VMM and DIC was proposed first for mode shapes characterization [36], and further extended to stereo-photogrammetry [37] proposing a 3D-DIC solution built on top of two individually magnified videos. Besides, quantitative variants of the VMM approach started to appear, with the ambition of not only magnifying the observed vibrations but also measuring the underlying motion [38]. Phase-based motion processing enabled the extraction of the operational deflection shapes of a wind turbine [39,40], and paved the way for the phase-based damage detection approach proposed later in [41]. An enhanced phase-based video processing method was recently proposed in [42], where authors demonstrated the superior quality obtained by using an Hilbert transform based approach, instead of the more traditional Gabor wavelet.

More recently, Yang et al. demonstrated the possibility of using a tuned version of the VMM original pipeline, without the need for any other measuring methods, nor the prior knowledge of the resonance frequencies, by exploiting blind source separation techniques for experimental modal analysis [43], high-fidelity finite element modal updating, and full-field dynamic strains estimation [44].

A similar research was presented recently in [45], which relies on DIC for retrieving experimentally a set of full-field strain mode shapes used to define a high-fidelity finite element (FE) model, and using it within a dedicated strain expansion–reduction approach. Other solutions achieving model-based strain estimation were previously attempted in [46], by using a few optical markers on the structure, and in [47,48], by exploiting a virtual sensing strategy jointly with a very limited number of accelerometers.

In view of the recent advances documented in [43,44], this work promotes the usage of VMM as an inspection tool for defect or damage detection. Vibration-based structural damage detection has been an active research field over the last decades, with several methods developed around the general idea of using the vibration response of the monitored structure to understand its overall structural health condition [49–52]. Since Pandey and colleagues have paved the way for damage detection based on observing the changes in the curvature of mode shapes [53], a plethora of works have investigated the subject [54–61]. The numerical issues challenging the applicability of the methods have been relaxed: the solution proposed in [58] relies on a modified Savitzky–Golay filter and the cubic smoothing spline method; whereas Yang et al. have more recently demonstrated robustness and efficiency of evaluating the modal curvature by exploiting the Fourier spectral method [59–61]. More importantly, the usage of mode shape derivatives has been mathematically and experimentally proven to be sensitive enough for obtaining a reference-free damage detection method.

Differently from the past, the above-mentioned progress in optical vibration methods offers unprecedented possibilities in the field of vibration-based damage detection. For this reason, we propose a modification of the VMM original pipeline [31], which relies on the 1D-Fourier transform for gathering the frequency spectrum, or a sparse subset of harmonics, of the Complex-Pyramid phase coefficients. The overall procedure relies on three steps. First, we extract the frequency response function (FRF) of a subset of small cropped regions of the video in order to estimate the dynamic response of the specimen under investigation, similarly to [38]. Afterwards, we execute a full-field computation of all the operational deflection shape pyramids. The latter may be properly collapsed into Image-space operational deflection shapes (ODSs). Finally, the first and second derivatives of each ODS are considered as damage indicators, which enables to highlight the presence of defects or damage, even using a single camera setup, and without requiring any knowledge of the healthy reference structure.

In particular, this work aims at demonstrating the feasibility of the proposed damage detection approach by looking into the following aspects: (1) verifying and assessing to what extent the considered levels of damage produce a significant difference in terms of operational deflection shapes, (2) investigating the effectiveness of the Complex-Steerable Pyramid decomposition as a tool for extracting both the phase-based FRF of the observed specimen, and (3) the full-field image-space deflection shapes; (4) probing the robustness of the proposed reference-free detection of defects. These feasibility tasks were performed by means of photo-realistic FEM simulations, conceived to mimic realistic experimental scenarios using different levels of damage, and with increasing levels of simulated noise. Numerical experiments allowed to conduct the feasibility investigation without the interference of other challenging effects, such as luminance variation or misalignment of the camera between the different testing conditions. In particular, the use of artificial video sequences enabled the explicit comparison of damaged vs. healthy structures, allowing a quantitative and objective evaluation of the severity of the simulated damage levels.

The remainder of the paper is structured as follows: Section 2 describes the proposed methodology, whereas results of the numerical feasibility assessment are presented in Section 3, and finally discussed in Section 4.

2. Phase-based defect detection

As depicted in Fig. 1, we exploit the complex steerable pyramid decomposition for its ability to make even the more subtle tiny motions of the sampled specimen detectable as a proportional phase-shifting of the complex coefficients. In practice, we adapted the original Phase-based Video motion processing [31], by exploiting the Discrete Fourier Transform (DFT), instead of band-pass filtering the phase-shifting time-series of each sub-band in the pyramid. In particular, we formulated these DFT operations to extract a small sparse subset of harmonics. The processing can be summarized as follows. Each image is transformed into its corresponding

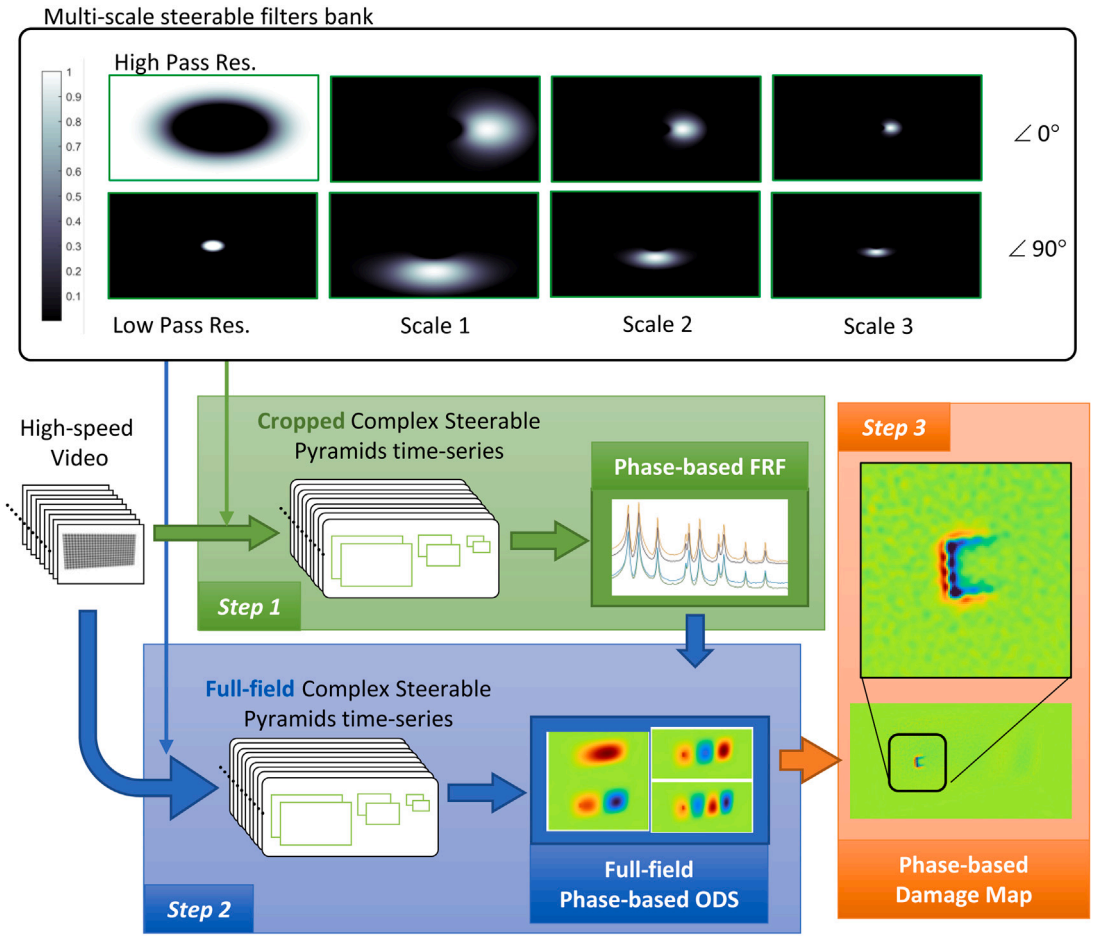

Fig. 1. An illustration of the proposed Phase-based Defect Detection process.

Complex Steerable Pyramid (CSP) [31]. Each video frame is convoluted with a set of multi-scale steerable filters. Each complex sub-band, $\mathbf{L}^i_{\theta,s}$, oriented along direction θ, and at scale s, can be decomposed as:

$$\mathbf{L}^i_{\theta,s} = \mathbf{M}^i_{\theta,s} e^{\mathbf{i}\mathbf{P}^i_{\theta,s}}. \tag{1}$$

where the two real-valued images, $\mathbf{M}^i_{\theta,s}$ and $\mathbf{P}^i_{\theta,s}$, represent respectively magnitude and phase of the corresponding sub-band level for the ith video frame. The size of each level depends on the originating frame size, and on the used kernel type. When using an octave-CSP, the first levels of the pyramid have the same size as the captured frame, with dimensions almost halving at every scale level. More details on the fundamental theory behind the CSP formulation can be found in [62,63]. Within this paper, each level of the CSP is stored without subsampling, thus maintaining the same resolution as the originating frame.

The variations of each complex steerable pyramids sub-band, $\Delta\mathbf{L}^i_{\theta,s}$, are obtained with respect to a designated reference frame, $\tilde{\mathbf{L}}_{\theta,s}$, exploiting the complex conjugate operator $()^*$, as follows:

$$\Delta\mathbf{L}^i_{\theta,s} = \Delta\mathbf{M}^i_{\theta,s} e^{\mathbf{i}\Delta\mathbf{P}^i_{\theta,s}} = \frac{\mathbf{L}^i_{\theta,s} \cdot \tilde{\mathbf{L}}^*_{\theta,s}}{\tilde{\mathbf{L}}_{\theta,s} \cdot \tilde{\mathbf{L}}^*_{\theta,s}} \tag{2}$$

It is worth noting that most of the computations represented in Eq. (2) can be efficiently organized by computing the complex gain matrix, $\tilde{\mathbf{K}}$, which depends only on the reference image,

$$\tilde{\mathbf{K}} = \frac{\tilde{\mathbf{L}}^*_{\theta,s}}{\tilde{\mathbf{L}}_{\theta,s} \cdot \tilde{\mathbf{L}}^*_{\theta,s}}. \tag{3}$$

As a result, the phase shifting signals, $\Delta\mathbf{P}^i_{\theta,s}$, are extracted by taking the argument of the complex-valued sub-bands:

$$\Delta\mathbf{P}^i_{\theta,s} = \arg(\Delta\mathbf{L}^i_{\theta,s}) = \arg(\mathbf{L}^i_{\theta,s} \cdot \tilde{\mathbf{K}}). \tag{4}$$

Considering N as the number of frames recorded in the video, the kth component of the DFT can be computed as:

$$\boldsymbol{\Phi}^{k}_{\theta,s} = \sum_{i=1}^{N} \Delta\mathbf{P}^{i}_{\theta,s} \mathrm{e}^{-\mathrm{i}2\pi \frac{(i-1)(k-1)}{N}}. \tag{5}$$

The phase-based video processing (Eq. (1)–(4)) enables to use each pixel of the video as a sensor array, more exactly one sensor for each subband of the pyramid. The sensitivity of each pixel sensor depends on the strength of the local texture and its orientation with respect to each filter direction. Similarly to the approach used in [64], a more robust estimate of the full-field spectral deformation shapes, $\boldsymbol{\Phi}^{k}$, is obtained as the weighted sum of each subband component:

$$\boldsymbol{\Phi}^{k} = \frac{\sum_{\theta,s} \boldsymbol{\Phi}^{k}_{\theta,s} \cdot \tilde{\mathbf{M}}^{2}_{\theta,s}}{\sum_{\theta,s} \tilde{\mathbf{M}}^{2}_{\theta,s}}. \tag{6}$$

The obtained spectral shapes are obtained exploiting the proportionality of the phase-shifting signals of each sub-bands to the true motion. It is worth mentioning that the Phase-based optical flow signals reported along this study are proportional to the module of the optical flow, which represents the velocity vector of each point of the observed specimen projected on the image plane. As a result, the reported signals maintain the dimension of angles, as we are reporting directly the phase-shift computed along each complex subband with respect to the reference frame.

2.1. Step 1: FRF computing

As a preliminary step, following an approach similar to [38], various cropped regions of the video are extracted and processed. Each region represents a sort of "virtual displacement sensor" which can be estimated applying Eqs. (1)–(6), in order to obtain the full-field single-sided spectrum, $\boldsymbol{\Phi}^{k}, \forall k = 0 \ldots \frac{N}{2}$. In particular, the phase-based optical flow FRF of the considered location is obtained as the sum of the magnitude of the obtained spectral components for each pixel belonging to the corresponding region of interest (ROI). Choice of the amount of cropped ROIs, and their location could follow the same criteria commonly used for achieving optimal sensor placement. In fact, a ROI centered around the stationary point of a certain eigenshape, may result in a poor estimation of the corresponding eigenfrequency. The size of the ROIs can be tuned in order to balance between computational efficiency and robustness. In facts, smaller ROI are computed faster; whereas bigger ROIs lead to more robust results, as they rely on a larger set of pixels.

2.2. Step 2: Extracting the full-field deflection shapes

The FRFs, obtained either by the method described at the previous section or by using conventional vibration testing equipment, are instrumental to accomplish a preliminary dynamic analysis, and more importantly to peak-pick the set of frequencies for which notable deflection shapes will be extracted using the proposed Video Motion Processing.

For each designated frequency, $\tilde{f}$, we obtain:

$$\tilde{k} = \lfloor \frac{\tilde{f}}{F_s} \rceil N, \tag{7}$$

where F_s is the sampling frequency, and $\tilde{k}$ is the integer index used to steer the sparse discrete Fourier transform computation of the corresponding ODS, $\tilde{\boldsymbol{\Phi}}$, obtained by evaluating Eqs. (5) and (6) at full-field resolution.

2.3. Step 3: Computing the damage maps

Similarly to [60], we exploit the Fourier domain for extracting the full-field derivatives of each ODS map. Considering the forward and inverse DFT applied to each ODS map, $\boldsymbol{\Phi}^{k}$:

$$\boldsymbol{\Theta}^{k} = \mathbf{DFT}(\boldsymbol{\Phi}^{k}) \Rightarrow \boldsymbol{\Theta}^{k}_{p+1,q+1} = \sum_{j=0}^{m-1} \sum_{i=0}^{n-1} \mathrm{e}^{-\mathrm{i}2\pi \frac{pj}{m} \frac{qi}{n}} \boldsymbol{\Phi}^{k}_{j+1,i+1}, \forall p = 0 \ldots m-1 \wedge \forall q = 0 \ldots n-1 \tag{8}$$

$$\boldsymbol{\Phi}^{k} = \mathbf{IDFT}(\boldsymbol{\Theta}^{k}) \Rightarrow \boldsymbol{\Phi}^{k}_{j+1,i+1} = \frac{1}{m}\frac{1}{n} \sum_{p=0}^{m-1} \sum_{q=0}^{n-1} \mathrm{e}^{\mathrm{i}2\pi \frac{pj}{m} \frac{qi}{n}} \boldsymbol{\Theta}^{k}_{p+1,q+1}, \forall j = 0 \ldots m-1 \wedge \forall i = 0 \ldots n-1 \tag{9}$$

the image-space second derivatives of each ODS map, can be obtained conveniently in the Fourier Domain, as follows:

$$\frac{\partial^2 \boldsymbol{\Phi}^{k}}{\partial x^2} = \mathbf{IDFT}\left(\boldsymbol{\Theta}^{k} \times K^{x} \times K^{x}\right); \tag{10}$$

$$\frac{\partial^2 \boldsymbol{\Phi}^{k}}{\partial y^2} = \mathbf{IDFT}\left(\boldsymbol{\Theta}^{k} \times K^{y} \times K^{y}\right); \tag{11}$$

where multiplications, $\times$, are intended pixel-by-pixel, and the derivative filters, K^{x} and K^{y}, are defined according to:

$$K^{x}_{j,i} = n\left[\mathrm{e}^{\mathrm{i}2\pi \frac{i-1}{n}} - 1\right]; \forall i = 1 \ldots n \wedge \forall j = 1 \ldots m \tag{12}$$

Table 1
Specimen geometry.

Name	Parameter	Value [mm]
Plate width	a	250
Plate height	b	500
Vertical position of the defect	c	125
Horizontal position of the defect	d	100
Vertical position of the exciting force	e	90
Horizontal position of the exciting force	f	150
Small Damage (S_1)	d_1	12
Medium Damage(S_2)	d_2	21
Big Damage (S_3)	d_3	30

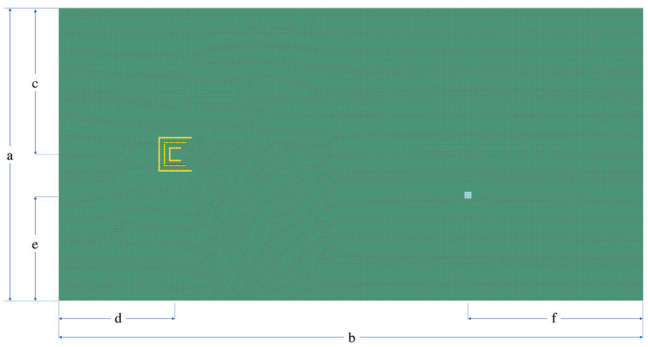

Fig. 2. Finite Element Model of the plate with different defect sizes.

$$K^{y}_{j,i} = n\left[\mathrm{e}^{\mathrm{i}2\pi\frac{j-1}{m}} - 1\right]; \forall i = 1 \dots n \wedge \forall j = 1 \dots m \tag{13}$$

Damage identification maps, $\mathbf{D}^k$, corresponding to the designated k-ith ODS frequency, are computed evaluating the second order spatial derivatives of each ODS map, $\boldsymbol{\Phi}^k$.

$$\mathbf{D}^k = \frac{\partial^2 \tilde{\boldsymbol{\Phi}}^k}{\partial x^2} + \frac{\partial^2 \boldsymbol{\Phi}^k}{\partial y^2}. \tag{14}$$

A broadband version of the above mentioned damage map indicator is obtained by summation of all the previously extracted ODSs:

$$\mathbf{D} = \sum_k \mathbf{D}^k. \tag{15}$$

3. Feasibility validations

A set of numerical investigations were carried out to assess potential and possible limitations of the Phase-based defect detection methodology presented in Section 2. All validation cases rely on the combination of advanced photo-realistic rendering techniques and FE dynamic simulations.

3.1. Simulation analysis case

Inspired by a recent experimental campaign [65], we modeled a rectangular aluminum plate, by means of the Siemens Simcenter 3D software package. Damaged versions of the same plate have been realized by removing different sets of elements, thus obtaining varying sizes of a C-shaped passing-through cut, as depicted also in Figs. 2 and 3. Geometrical parameters of the specimen, and of the different damages are detailed in Table 1.

After imposing the essential boundary conditions on the four clamped edges of the plate, we extracted the modal parameters by means of the real eigenvalue analysis module (SOL 103 Flexible Body), for each variant of the plate.

The same mesh used for the FEM analysis was used to build a tessellated polygonal object within an OpenGL 3D rendering context. To mimic the textured effect of the real specimen, a gray-color pattern with a smoothly varying texture was generated by tuning properly the raster shading rendering stage, which is the program within modern GPU rendering pipelines responsible for computing the color of each pixel before appearing on the screen. In practice, the gray-level color c (black: c=0; white: c=1.0) of each point was coded as a function of its location within the plate, in order to mimic a multi-wavelength texture coating. This was achieved according to the following formula:

$$c = 0.1 + 0.4\cos^2\left(\frac{2\pi}{\lambda}x\right) + 0.4\sin^2\left(\frac{2\pi}{\lambda}y\right) \tag{16}$$

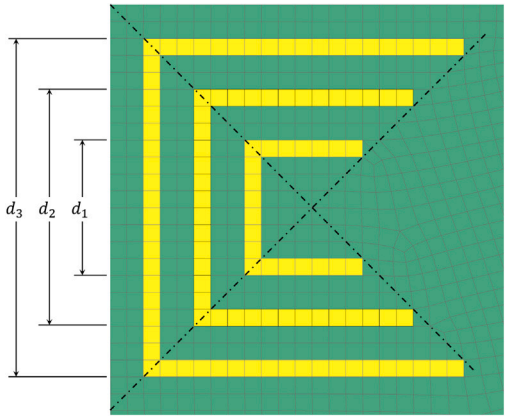

Fig. 3. Varying sizes of the considered damage.

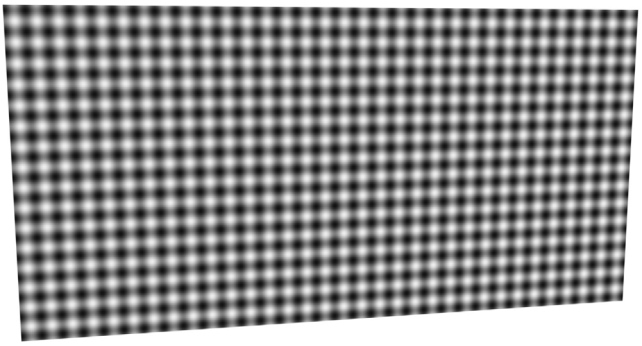

Fig. 4. Photorealistic rendering of the simulated plate.

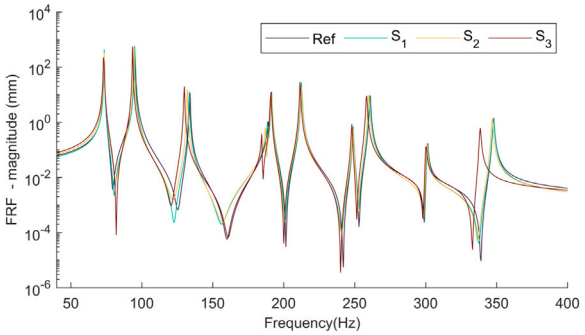

Fig. 5. FRF displacements extracted from FE simulations at the impact location.

where the wavelength of the texture, λ, was tuned as

$$\lambda = \frac{500}{33}\ \text{mm}. \tag{17}$$

The resulting photorealistic plate model is depicted in Fig. 4.

Animation of the photorealistic plates, required for producing the videos of the vibrating panels was obtained by updating the position of the nodes of the underlying tessellation. First, we solved the transient dynamic analysis of the underlying FE of the plate specimens, subject to an impulse force applied at the location depicted in Fig. 2. Fig. 5 exemplifies such responses for the impact node location.

Secondly, the simulated modal displacements were used as input on the dedicated modal-based rendering program. For the scope of this work, the simulated videos of each damaged plate were stored using 8-bit gray levels uncompressed image sequences, of 512x1024 pixel resolution. Moreover, each frame of the obtained reference videos was contaminated with four levels of additive

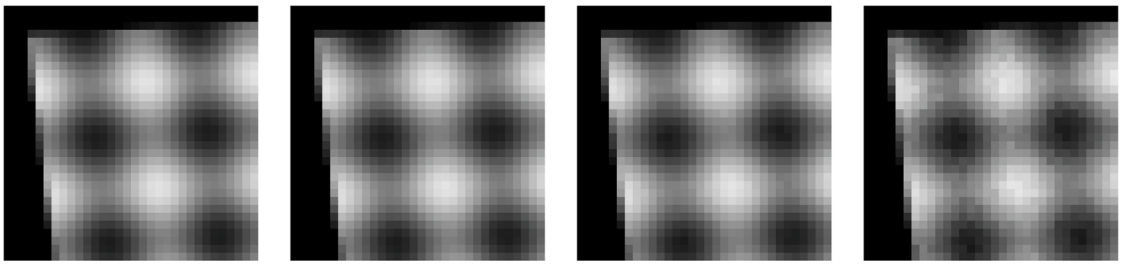

(a) $\sigma = 0.5$ (b) $\sigma = 1.0$ (c) $\sigma = 2.0$ (d) $\sigma = 5.0$

Fig. 6. A detailed view of the top-left corner of the simulated plate, recorded emulating four levels of additive Gaussian random noise, with a standard deviation of $\sigma = [0.5, 1.0, 2.0, 5.0]$ 8bit-gray levels.

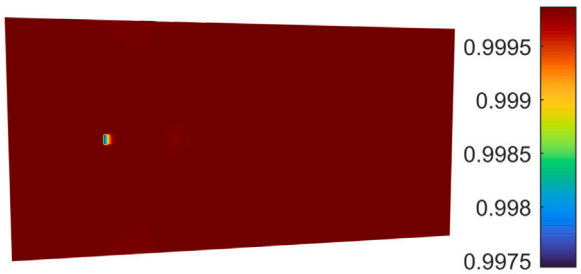

(a) COMAC - S_1

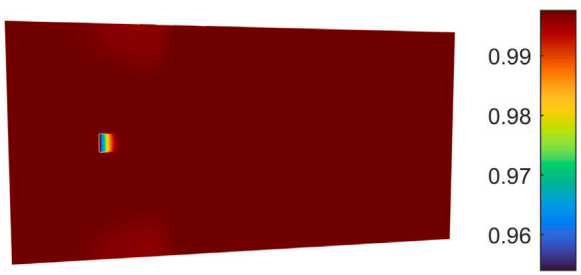

(b) COMAC - S_2

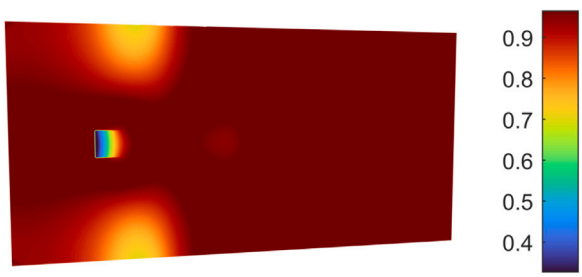

(c) COMAC - S_3

Fig. 7. COMAC damage metric computed for different size of the considered defect by using the eigen shapes from the FE Analysis.

normally distributed zero-mean random noise, with a standard deviation of $\sigma = [0.5, 1.0, 2.0, 5.0]$ 8bit-gray levels. The impact of the chosen noise levels in deteriorating the image quality is exemplified in Fig. 6.

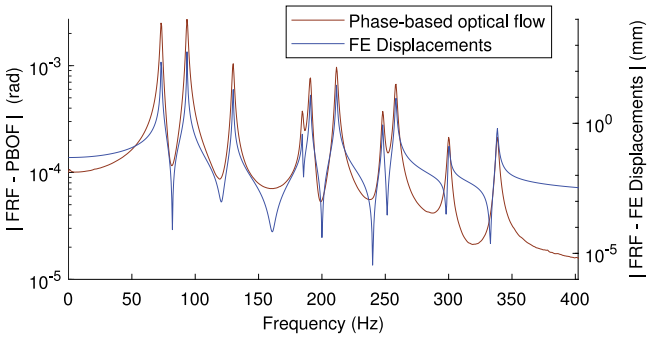

Fig. 8. Validation of the phase-based FRF, in comparison with the FRF obtained from the FE simulations.

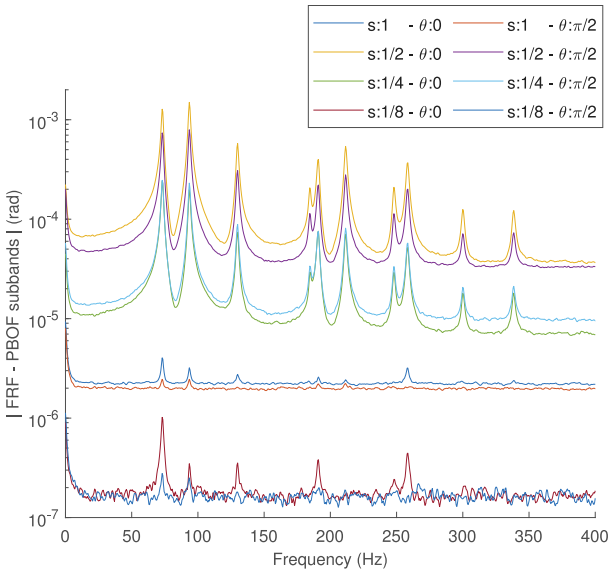

Fig. 9. Contributions of each sub-band to the phase-based FRF computations.

3.2. Assessing the level of damage

A simple, yet well established metric used to identify and locate damage in term of modification to the mode shapes is the coordinate modal assurance criterion (COMAC) [50], which can be evaluated as:

$$\mathbf{COMAC}_i = \frac{\left(\sum_{j=1}^{m} \boldsymbol{\phi}_{i,j}^{u} \boldsymbol{\phi}_{i,j}^{d}\right)^2}{\left(\sum_{j=1}^{m} (\boldsymbol{\phi}_{i,j}^{u})^2\right)\left(\sum_{j=1}^{m} (\boldsymbol{\phi}_{i,j}^{d})^2\right)} \tag{18}$$

where $\boldsymbol{\phi}_{i,j}^{u}$ and $\boldsymbol{\phi}_{i,j}^{d}$ represent the jth eigen vectors, evaluated at each point i on the healthy and on the damaged structure respectively.

As reported in Fig. 7, the three defect sizes, S_1, S_2, S_3, produce an impact on the COMAC index, with most of the reduction localized around the defect location. As expected, the largest defect, S_3, produced the biggest damage, with a considerable COMAC reduction of above 60% around the defect location, whereas the smaller defects, S_1 and S_2, procured respectively a COMAC reduction of about 0.25% and 4.5%.

3.3. Phase-based FRF

A cropped region of 256x256 pixels centered around the impact point has been selected for the scope of applying the method detailed in Section 2.1, thus computing the phase-based FRF around the simulated impact location.

The quality of the obtained phase-based FRF was validated in comparison with the FRF extracted from the corresponding FE simulation. Fig. 8 exemplifies such a validation for the S_3 defect size case.

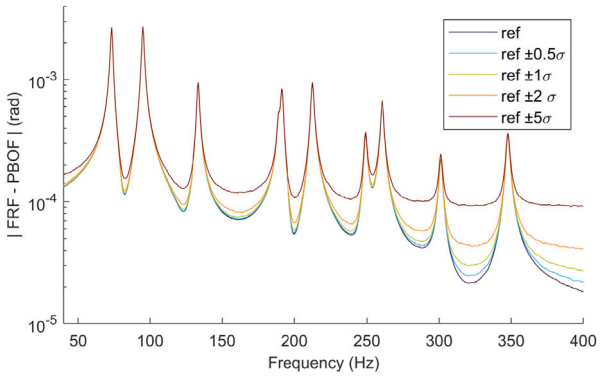

Fig. 10. Phase-based Optical Flow FRF estimated around the impact location for the S_1 defect size, under increasing level of noise.

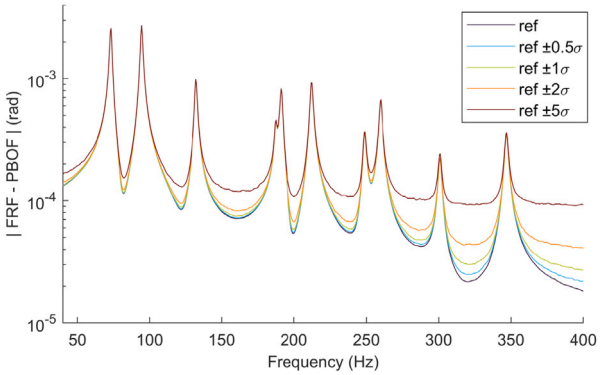

Fig. 11. Phase-based Optical Flow FRF estimated around the impact location for the S_2 defect size, under increasing level of noise.

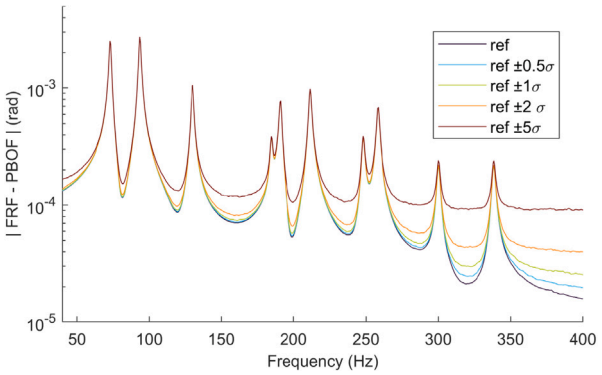

Fig. 12. Phase-based Optical Flow FRF estimated around the impact location for the S_3 defect size, under increasing level of noise.

To better understand the effectiveness of the Complex-Steerable Pyramid decomposition, Fig. 9 reports the contribution of each subband to the overall computation of the FRF. It is interesting to note that subbands of different scales contribute with different levels of significance, spanning several orders of magnitude.

The FRF extraction procedure has been repeated for every defect size and for all the considered levels of noise. The corresponding results are documented in Figs. 10–12.

3.4. Full-field operational deflection shapes

As described in Section 2.2, the frequencies for the extraction of the corresponding full-field ODSs were selected by pick-picking on the obtained phase-based FRF results. A summary of all the selected frequencies is reported in Table 2, alongside the corresponding eigen-frequencies obtained by means of FE analysis. The resulting full-field ODSs are depicted in Fig. 13.

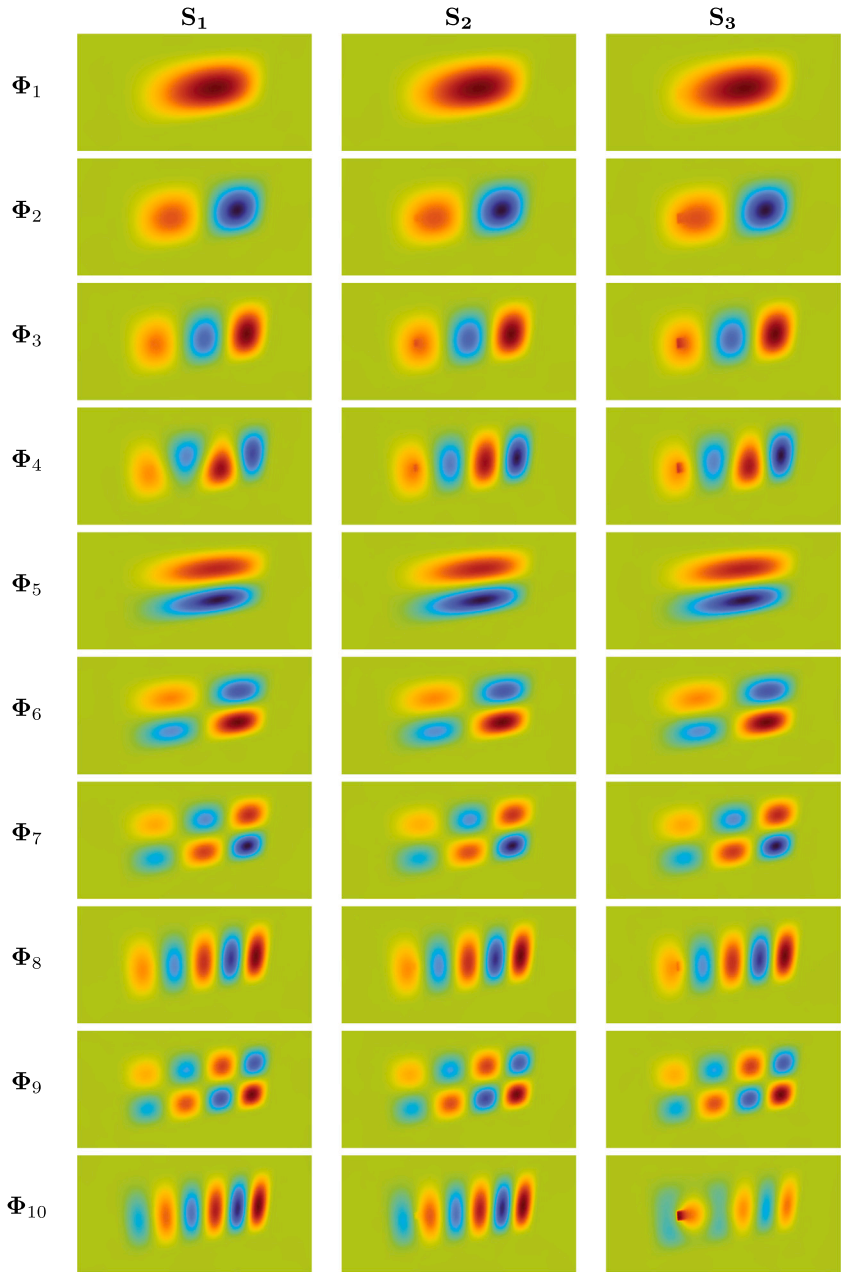

Fig. 13. ODSs extracted using phase-based motion processing.

3.5. Damage map indicators

Damage indicators for the three different sizes of the defect were computed as described in Section 2.3. Fig. 14 depicts the obtained results. For all the reported results, the pseudo-color scaling has been automatically adjusted to maximize contrast.

As expected the damage indicator has a very neat result for the biggest damage case, with all ODSs contributing clearly to the final result, except the seventh and the ninth ones. For the smaller damage, $\mathbf{S_2}$, the contours of the smaller defect are still apparent in the final result, although with less contrast. It is also interesting to note that only a subset (namely the 2nd, 3rd, 4th, 8th and 10th) of all the considered ODSs have a significant contribution to the final results. As expected, the proposed method was not able to achieve a significant result for the smallest defect. However, such a result is in line with the predicted severity of the damage, as discussed in Section 3.2. The comparison of the obtained results suggests that the proposed curvature-based damage index is also proportional to the severity of the defect.

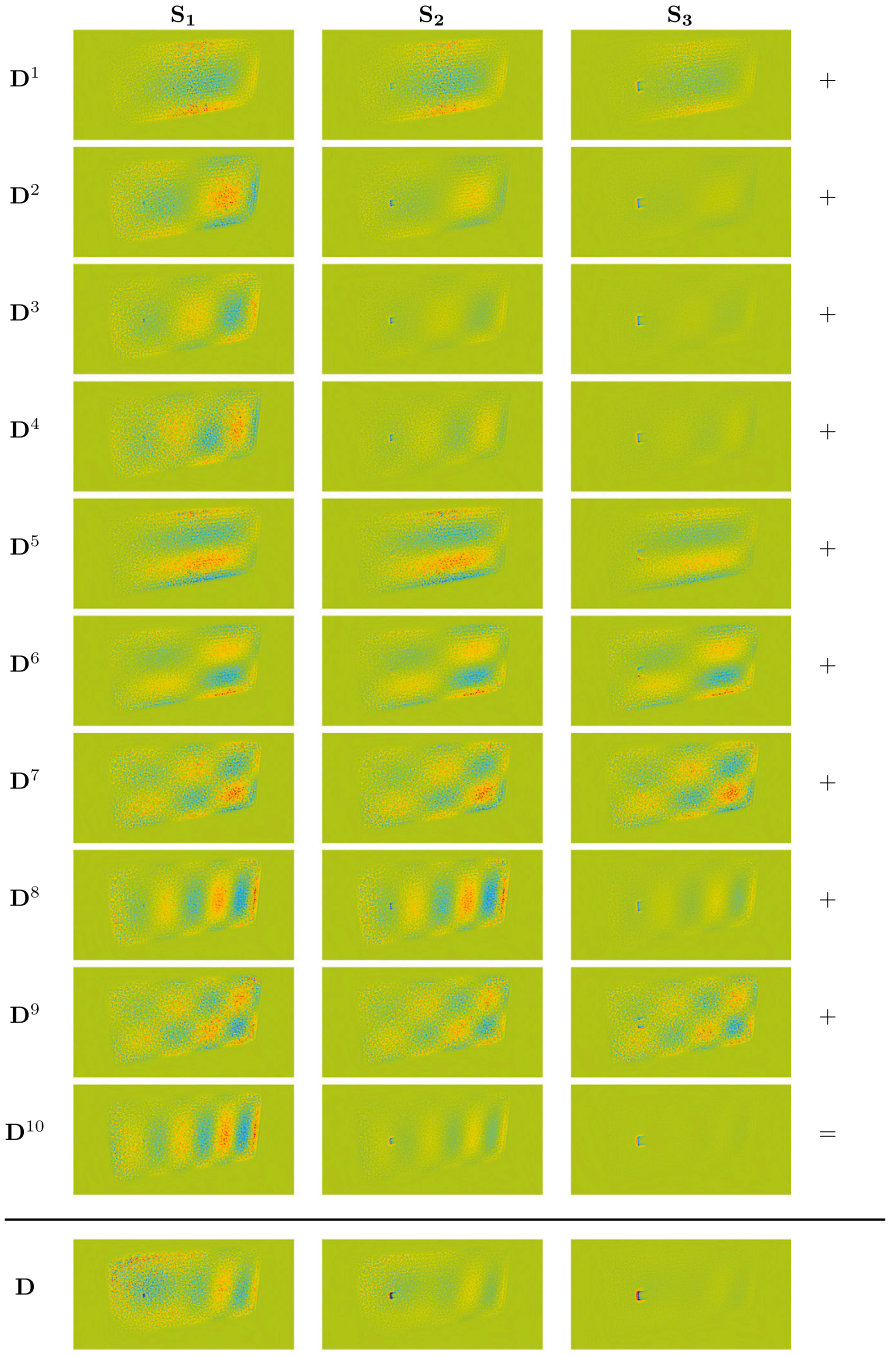

Fig. 14. Modal Curvature Damage maps ODS extracted using phase-based motion processing.

3.6. Damage map indicators: sensitivity to noise effects

As reported in Fig. 15, our results indicate that the considered curvature-based damage indicators are quite robust against noise effects. Generally speaking, noise can be tolerated quite well. For the biggest damage case, S_3, defect is neatly identified even with the highest noise levels, which may correspond to extremely poor illumination conditions. In similar circumstances, the proposed procedure became incapable of detecting the smaller defect, S_2. Noise effects for the smallest damage scenario, S_1, were not investigated.

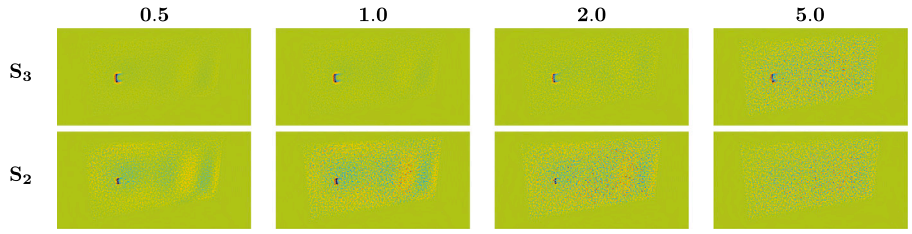

Fig. 15. Modal Curvature Damage maps extracted using phase-based motion processing, for increasing levels of noise in the recorded video.

Table 2
Finite Element (FE) eigen-frequencies vs. Phase Based (PB) Peak-frequency (see Section 2.1), for three different defect sizes: $\mathbf{S}_1$, $\mathbf{S}_2$, $\mathbf{S}_3$. All frequency are expressed in Hz.

Mode N.	S_1:FE	S_1:PB	S_2:FE	S_2:PB	S_3:FE	S_3:PB
1	73.4597	73.5	73.3718	73.5	73.2189	73.0
2	94.9715	95.0	94.4696	94.5	93.5524	93.5
3	133.3623	133.5	132.1067	132.0	129.8549	130.0
4	188.7511	189.0	187.2650	187.5	184.5926	184.5
5	191.2743	191.0	191.1609	191.0	190.8529	191.0
6	212.4478	212.5	212.2180	212.5	211.5282	211.5
7	248.9064	249.0	248.6990	249.0	247.9912	248.0
8	260.6073	260.5	259.8465	260.0	258.2970	258.5
9	301.1633	301.0	300.8490	301.0	300.1411	300.0
10	347.7249	348.0	346.8345	347.0	338.3573	338.5

4. Conclusions

In this work we presented a novel defect detection methodology aiming at exploiting the advantages of phase-based motion magnification in combination with a reference-free damage localization procedure. The conceived methodology consists of two phases: first, the eigen-frequencies are deduced from post-processing the phase-based optical flow signals or alternatively the accelerometer and shaker or hammer excitation signals; afterwards, the operational deflection shapes (ODSs) corresponding to each eigen-frequency are extracted using a revised version of the original phase-based motion magnification pipeline, which we conceived to extract the FRF harmonics, one for each frequency of interest, and coded as complex steerable pyramids. Defect detection is achieved by analyzing the curvature of the extracted ODSs. Numerical investigations were carried out by means of the photorealistic FEM model of a fully clamped plate.

The reported results confirmed that all the modal full-field high resolution ODSs in a prescribed bandwidth can be extracted. In particular, the defect detection can be achieved by monitoring the extracted ODSs, despite considering a single-view scenario.

Furthermore, feasibility of the damage detection was assessed for different sizes of the defect. An estimation of the severity of the defects was proposed by means of the COMAC criterion. Moreover we demonstrated the robustness of the procedure against noise.

Data availability

Data will be made available on request.

Acknowledgments

The research of Francesco Cosco was partially funded by the European Commission - FSE and FESR, within the PON R&I 2014–2020 program, Action I.2 Attraction and International Mobility (AIM1857122); This work is part of research project DETECT-ION, funded by Flanders innovation agency VLAIO under SIM program M3.

References

[1] J. Baqersad, P. Poozesh, C. Niezrecki, P. Avitabile, Photogrammetry and optical methods in structural dynamics – A review, Mech. Syst. Signal Process. 86 (2017) 17–34, http://dx.doi.org/10.1016/j.ymssp.2016.02.011.

[2] A. Zanarini, Full field optical measurements in experimental modal analysis and model updating, J. Sound Vib. 442 (2019) 817–842, http://dx.doi.org/10.1016/j.jsv.2018.09.048.

[3] C. Warren, P. Pingle, C. Niezrecki, P. Avitabile, Comparison of image based, laser, and accelerometer measurements, in: Conf Proc Soc Exp Mech Series, vol. 3, 2011, pp. 15–21, http://dx.doi.org/10.1007/978-1-4419-9834-7_2.

[4] Y.F.F. Xu, A photogrammetry-based experimental modal analysis method by tracking visible laser spots, Measurement 151 (2020) http://dx.doi.org/10.1016/j.measurement.2019.106963.

[5] P.L. Reu, D.P. Rohe, L.D. Jacobs, Comparison of DIC and LDV for practical vibration and modal measurements, Mech. Syst. Signal Process. 86 (2017) 2–16, http://dx.doi.org/10.1016/j.ymssp.2016.02.006.

[6] A. Zanarini, Competing optical instruments for the estimation of full field FRFs, Measurement 140 (2019) 100–119, http://dx.doi.org/10.1016/j.measurement.2018.12.017.

[7] B.K.P. Horn, B.G. Schunck, Determining optical flow, in: Artificial Intelligence in Perspective, The MIT Press, 1994, pp. 185–203, http://dx.doi.org/10.7551/mitpress/1413.003.0014.

[8] B.D. Lucas, T. Kanade, Iterative image registration technique with an application to stereo vision., in: Proc. 7th Intl Joint Conf on Artificial Intelligence (IJCAI), vol. 2, Morgan Kaufmann Publishers Inc., 1981, pp. 674–679.

[9] D.J. Fleet, A.D. Jepson, Computation of component image velocity from local phase information, Int. J. Comput. Vis. 5 (1990) 77–104, http://dx.doi.org/10.1007/BF00056772.

[10] J. Javh, J. Slavič, M. Boltežar, The subpixel resolution of optical-flow-based modal analysis, Mech. Syst. Signal Process. 88 (2017) 89–99, http://dx.doi.org/10.1016/j.ymssp.2016.11.009.

[11] J. Javh, J. Slavič, M. Boltežar, High frequency modal identification on noisy high-speed camera data, Mech. Syst. Signal Process. 98 (2018) 344–351, http://dx.doi.org/10.1016/j.ymssp.2017.05.008.

[12] Y. Wang, F.S. Egner, T. Willems, M. Kirchner, W. Desmet, Camera-based experimental modal analysis with impact excitation: Reaching high frequencies thanks to one accelerometer and random sampling in time, Mech. Syst. Signal Process. 170 (2022) 108879, http://dx.doi.org/10.1016/j.ymssp.2022.108879.

[13] D.H. Diamond, P.S. Heyns, A.J. Oberholster, Accuracy evaluation of sub-pixel structural vibration measurements through optical flow analysis of a video sequence, Measurement 95 (2017) 166–172, http://dx.doi.org/10.1016/j.measurement.2016.10.021.

[14] I. Tomac, J. Slavič, Damping identification based on a high-speed camera, Mech. Syst. Signal Process. 166 (2022) 108485, http://dx.doi.org/10.1016/j.ymssp.2021.108485.

[15] X.W. Ye, T.H. Yi, C.Z. Dong, T. Liu, Vision-based structural displacement measurement: System performance evaluation and influence factor analysis, Measurement 88 (2016) 372–384, http://dx.doi.org/10.1016/j.measurement.2016.01.024.

[16] A. Sarrafi, P. Poozesh, Z. Mao, A comparison of computer-vision-based structural dynamics characterizations, in: Conf Proc Soc Exp Mech Series, vol. 3 Part F2, Springer New York LLC, 2017, pp. 295–301, http://dx.doi.org/10.1007/978-3-319-54858-6_29.

[17] T. Durand-Texte, E. Simonetto, S. Durand, M. Melon, M.-H.H. Moulet, Vibration measurement using a pseudo-stereo system, target tracking and vision methods, Mech. Syst. Signal Process. 118 (2019) 30–40, http://dx.doi.org/10.1016/j.ymssp.2018.08.049.

[18] W. Wang, X. Li, A. Chen, A method of modal parameter identification for wind turbine blade based on binocular dynamic photogrammetry, Shock Vib. 2019 (2019) http://dx.doi.org/10.1155/2019/7610930.

[19] S. Barone, P. Neri, A. Paoli, A.V. Razionale, Low-frame-rate single camera system for 3D full-field high-frequency vibration measurements, Mech. Syst. Signal Process. 123 (2019) 143–152, http://dx.doi.org/10.1016/j.ymssp.2019.01.016.

[20] W. Wang, J.E. Mottershead, T. Siebert, A. Pipino, Frequency response functions of shape features from full-field vibration measurements using digital image correlation, Mech. Syst. Signal Process. 28 (2012) 333–347, http://dx.doi.org/10.1016/j.ymssp.2011.11.023.

[21] P. Poozesh, J. Baqersad, C. Niezrecki, P. Avitabile, A multi-camera stereo DIC system for extracting operating mode shapes of large scale structures, in: Conf Proc Soc Exp Mech Series, vol. 3, Springer New York LLC, 2016, pp. 225–238, http://dx.doi.org/10.1007/978-3-319-22446-6_29.

[22] P. Castellini, P. Chiariotti, M. Martarelli, E. Zappa, A. Lavatelli, Experimental modal analysis on vibration data measured by digital image correlation, in: Conf Proc Soc Exp Mech Series, vol. 9B, Springer New York LLC, 2017, pp. 285–291, http://dx.doi.org/10.1007/978-3-319-54735-0_30.

[23] A. Lavatelli, E. Zappa, A displacement uncertainty model for 2-D DIC measurement under motion blur conditions, IEEE Trans. Instrum. Meas. 66 (2017) 451–459, http://dx.doi.org/10.1109/TIM.2016.2644898.

[24] A. Mange, J. Baqersad, V. Srivastava, J. More, Using digital image correlation to measure dynamics of rolling tires, in: SAE Technical Papers, SAE International, 2018, pp. 1–7, http://dx.doi.org/10.4271/2018-01-1217, https://www.sae.org/content/2018-01-1217/.

[25] V. Srivastava, K. Patil, J. Baqersad, J. Zhang, A multi-view DIC approach to extract operating mode shapes of structures, in: Conf Proc Soc Exp Mech Series, vol. 6, Springer International Publishing, 2019, pp. 43–48, http://dx.doi.org/10.1007/978-3-319-74476-6_6.

[26] D. Uehara, J. Sirohi, Full-field optical deformation measurement and operational modal analysis of a flexible rotor blade, Mech. Syst. Signal Process. 133 (2019) http://dx.doi.org/10.1016/j.ymssp.2019.106265.

[27] S. Barone, P. Neri, A. Paoli, A.V. Razionale, L. Bertini, C. Santus, Optical stereo-system for full-field high-frequency 3D vibration measurements based on low-frame-rate cameras, in: Lecture Notes in Mechanical Engineering, Springer, 2020, pp. 155–164, http://dx.doi.org/10.1007/978-3-030-31154-4_14.

[28] T. Durand-Texte, M. Melon, E. Simonetto, S. Durand, M.H.M.-H. Moulet, Single-camera single-axis vision method applied to measure vibrations, J. Sound Vib. 465 (2020) 115012, http://dx.doi.org/10.1016/j.jsv.2019.115012.

[29] R. Del Sal, L. Dal Bo, E. Turco, A. Fusiello, A. Zanarini, R. Rinaldo, P. Gardonio, Structural vibration measurement with multiple synchronous cameras, Mech. Syst. Signal Process. 157 (2021) 107742, http://dx.doi.org/10.1016/j.ymssp.2021.107742.

[30] F. Cosco, J. Cuenca, W. Desmet, K. Janssens, D. Mundo, On the usability of phase-based video motion magnification for defect detection in vibrating panels, in: Proc. of ISMA 2020 and USD 2020, KU Leuven, Leuven, 2020, pp. 2321–2331.

[31] N. Wadhwa, M. Rubinstein, F. Durand, W.T. Freeman, Phase-based video motion processing, ACM Trans. Graph. 32 (2013) http://dx.doi.org/10.1145/2461912.2461966.

[32] N. Wadhwa, M. Rubinstein, F. Durand, W.T. Freeman, Riesz Pyramids for fast phase-based video magnification, in: 2014 IEEE International Conference on Computational Photography, ICCP 2014, IEEE Computer Society, 2014, pp. 1–10, http://dx.doi.org/10.1109/ICCPHOT.2014.6831820.

[33] M.A. Elgharib, M. Hefeeda, F. Durand, W.T. Freeman, Video magnification in presence of large motions, in: Proc. IEEE CVPR, vol. 07-12-June-2015, IEEE Computer Society, 2015, pp. 4119–4127, http://dx.doi.org/10.1109/CVPR.2015.7299039.

[34] N. Wadhwa, J.G. Chen, J.B. Sellon, D. Wei, M. Rubinstein, R. Ghaffari, D.M. Freeman, O. Büyüköztürk, P. Wang, S. Sun, S.H. Kang, K. Bertoldi, F. Durand, W.T. Freeman, Motion microscopy for visualizing and quantifying small motions, Proc. Natl. Acad. Sci. USA 114 (2017) 11639–11644, http://dx.doi.org/10.1073/pnas.1703715114.

[35] P. Poozesh, A. Sarrafi, Z. Mao, P. Avitabile, C. Niezrecki, Feasibility of extracting operating shapes using phase-based motion magnification technique and stereo-photogrammetry, J. Sound Vib. 407 (2017) 350–366, http://dx.doi.org/10.1016/j.jsv.2017.06.003.

[36] A.J.J. Molina-Viedma, L. Felipe-Sesé, E. López-Alba, F. Díaz, High frequency mode shapes characterisation using digital image correlation and phase-based motion magnification, Mech. Syst. Signal Process. 102 (2018) 245–261, http://dx.doi.org/10.1016/j.ymssp.2017.09.019.

[37] A.J. Molina-Viedma, L. Felipe-Sesé, E. López-Alba, F.A. Díaz, 3D mode shapes characterisation using phase-based motion magnification in large structures using stereoscopic DIC, Mech. Syst. Signal Process. 108 (2018) 140–155, http://dx.doi.org/10.1016/j.ymssp.2018.02.006.

[38] J.G. Chen, N. Wadhwa, Y.J. Cha, F. Durand, W.T. Freeman, O. Buyukozturk, Modal identification of simple structures with high-speed video using motion magnification, J. Sound Vib. 345 (2015) 58–71, http://dx.doi.org/10.1016/j.jsv.2015.01.024.

[39] A. Sarrafi, Z. Mao, C. Niezrecki, P. Poozesh, Vibration-based damage detection in wind turbine blades using phase-based motion estimation and motion magnification, J. Sound Vib. 421 (2018) 300–318, http://dx.doi.org/10.1016/j.jsv.2018.01.050.

[40] A. Sarrafi, Z. Mao, Mapping motion-magnified videos to operating deflection shape vectors using particle filters, in: Conf Proc Soc Exp Mech Series, Springer International Publishing, 2019, pp. 75–83, http://dx.doi.org/10.1007/978-3-030-12935-4_8.

[41] A. Sarrafi, P. Poozesh, C. Niezrecki, Z. Mao, Detection of natural frequency and mode shape correspondence using phase-based video magnification in large-scale structures, in: Conf Proc Soc Exp Mech Series, vol. 6, Springer International Publishing, 2019, pp. 81–87, http://dx.doi.org/10.1007/978-3-319-74476-6_12.
[42] G. Liu, M.Z. Li, Z. Mao, Q.S. Yang, Structural motion estimation via Hilbert transform enhanced phase–based video processing, Mech. Syst. Signal Process. 166 (2022) 108418, http://dx.doi.org/10.1016/j.ymssp.2021.108418.
[43] Y. Yang, C. Dorn, T. Mancini, Z. Talken, G. Kenyon, C. Farrar, D. Mascarenas, Blind identification of full-field vibration modes from video measurements with phase-based video motion magnification, Mech. Syst. Signal Process. 85 (2017) 567–590, http://dx.doi.org/10.1016/j.ymssp.2016.08.041.
[44] Y. Yang, H.K. Jung, C. Dorn, G. Park, C. Farrar, D. Mascarenas, Estimation of full-field dynamic strains from digital video measurements of output–only beam structures by video motion processing and modal superposition, Struct. Control. Health Monit. 26 (2019) http://dx.doi.org/10.1002/stc.2408.
[45] K. Bharadwaj, A. Sheidaei, A. Afshar, J. Baqersad, Full-field strain prediction using mode shapes measured with digital image correlation, Measurement 139 (2019) 326–333, http://dx.doi.org/10.1016/j.measurement.2019.03.024.
[46] J. Baqersad, C. Niezrecki, P. Avitabile, Extracting full-field dynamic strain on a wind turbine rotor subjected to arbitrary excitations using 3D point tracking and a modal expansion technique, J. Sound Vib. 352 (2015) 16–29, http://dx.doi.org/10.1016/j.jsv.2015.04.026.
[47] F. Naets, F. Cosco, W. Desmet, An extended Kalman filter approach for augmented strain/stress visualization in mechanical systems, in: 2014 IEEE/ASME 10th International Conference on Mechatronic and Embedded Systems and Applications (MESA), IEEE, 2014, pp. 1–6, http://dx.doi.org/10.1109/MESA.2014.6935584.
[48] F. Naets, F. Cosco, W. Desmet, Improved human-computer interaction for mechanical systems design through augmented strain/stress visualisation, Int. J. Intell. Eng. Inform. 5 (2017) 50–66, http://dx.doi.org/10.1504/IJIEI.2017.082565.
[49] A. Alvandi, C. Cremona, Assessment of vibration-based damage identification techniques, J. Sound Vib. 292 (2006) 179–202.
[50] F.L.M. Dos Santos, B. Peeters, H. Van Der Auweraer, L.C.S. Góes, W. Desmet, Vibration-based damage detection for a composite helicopter main rotor blade, Case Stud. Mech. Syst. Signal Process. 3 (2016) 22–27, http://dx.doi.org/10.1016/j.csmssp.2016.01.001.
[51] O. Avci, O. Abdeljaber, S. Kiranyaz, M. Hussein, M. Gabbouj, D.J. Inman, A review of vibration-based damage detection in civil structures: From traditional methods to machine learning and deep learning applications, Mech. Syst. Signal Process. 147 (2021) 107077.
[52] J.J. Moughty, J.R. Casas, A state of the art review of modal-based damage detection in bridges: Development, challenges, and solutions, Appl. Sci. 7 (2017) 510, http://dx.doi.org/10.3390/app7050510.
[53] A.K. Pandey, M. Biswas, M.M. Samman, Damage detection from changes in curvature mode shapes, J. Sound Vib. 145 (1991) 321–332, http://dx.doi.org/10.1016/0022-460x(91)90595-b.
[54] P. Qiao, K. Lu, W. Lestari, J. Wang, Curvature mode shape-based damage detection in composite laminated plates, Compos. Struct. 80 (2007) 409–428, http://dx.doi.org/10.1016/j.compstruct.2006.05.026.
[55] K. Roy, S. Ray-Chaudhuri, Fundamental mode shape and its derivatives in structural damage localization, J. Sound Vib. 332 (2013) 5584–5593, http://dx.doi.org/10.1016/j.jsv.2013.05.003.
[56] K. Roy, Structural damage identification using mode shape slope and curvature, J. Eng. Mech. 143 (2017) 04017110, http://dx.doi.org/10.1061/(asce)em.1943-7889.0001305.
[57] V.B. Dawari, G.R. Vesmawala, Modal curvature and modal flexibility methods for honeycomb damage identification in reinforced concrete beams, Procedia Eng. 51 (2013) 119–124, http://dx.doi.org/10.1016/j.proeng.2013.01.018.
[58] G. Quaranta, B. Carboni, W. Lacarbonara, Damage detection by modal curvatures: numerical issues, J. Vib. Control 22 (2016) 1913–1927.
[59] Z.-B. Yang, M. Radzienski, P. Kudela, W. Ostachowicz, Two-dimensional modal curvature estimation via Fourier spectral method for damage detection, Compos. Struct. 148 (2016) 155–167, http://dx.doi.org/10.1016/j.compstruct.2016.04.001.
[60] Z.-B. Yang, M. Radzienski, P. Kudela, W. Ostachowicz, Fourier spectral-based modal curvature analysis and its application to damage detection in beams, Mech. Syst. Signal Process. 84 (2017) 763–781, http://dx.doi.org/10.1016/j.ymssp.2016.07.005.
[61] Z.-B. Yang, M. Radzienski, P. Kudela, W. Ostachowicz, Two-dimensional Chebyshev pseudo spectral modal curvature and its application in damage detection for composite plates, Compos. Struct. 168 (2017) 372–383, http://dx.doi.org/10.1016/j.compstruct.2017.02.066.
[62] E.P. Simoncelli, W.T. Freeman, E.H. Adelson, D.J. Heeger, Shiftable multiscale transforms, IEEE Trans. Inform. Theory 38 (1992) 587–607, http://dx.doi.org/10.1109/18.119725.
[63] J. Portilla, E.P. Simoncelli, Parametric texture model based on joint statistics of complex wavelet coefficients, Int. J. Comput. Vis. 40 (2000) 49–71, http://dx.doi.org/10.1023/A:1026553619983.
[64] N. Wadhwa, Revealing and analyzing imperceptible deviations in images and videos (Ph.D. thesis), Massachusetts Institute of Technology, 2016.
[65] N. Auquier, J. Cuenca, L. de Ryck, Coherence-based nearfield acoustic holography for damage detection in plates, in: Proc. of ISMA 2020 and USD 2020, 2020, pp. 2899–2907.